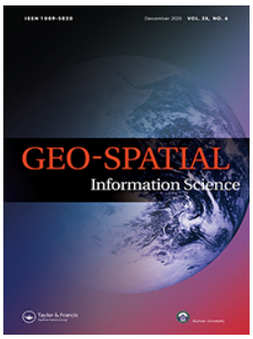

Geo-spatial Information Science

ISSN: 1009-5020 (Print) 1993-5153 (Online) Journal homepage: www.tandfonline.com/journals/tgsi20

Multi-dimensional dynamic deformation monitoring of long-span railway bridges using GBIR and IVM data fusion

Yuhao Liu, Songbo Wu, Bochen Zhang, Zhen Peng, Jiayuan Zhang, Chisheng Wang, Wei Tu, Zhipeng Chen, Mi Jiang, Xiao Cheng, Jiasong Zhu & Qingquan Li

To cite this article: Yuhao Liu, Songbo Wu, Bochen Zhang, Zhen Peng, Jiayuan Zhang, Chisheng Wang, Wei Tu, Zhipeng Chen, Mi Jiang, Xiao Cheng, Jiasong Zhu & Qingquan Li (2025) Multi-dimensional dynamic deformation monitoring of long-span railway bridges using GBIR and IVM data fusion, Geo-spatial Information Science, 28:6, 3057-3073, DOI: 10.1080/10095020.2025.2486282

To link to this article: https://doi.org/10.1080/10095020.2025.2486282

Published online: 08 Apr 2025.

GEO-SPATIAL INFORMATION SCIENCE
2025, VOL. 28, NO. 6, 3057–3073
https://doi.org/10.1080/10095020.2025.2486282

Multi-dimensional dynamic deformation monitoring of long-span railway bridges using GBIR and IVM data fusion

Yuhao Liu[a,b,c], Songbo Wu[c,d], Bochen Zhang[a,b], Zhen Peng[a,b], Jiayuan Zhang[a,b], Chisheng Wang[a,e], Wei Tu[a,e], Zhipeng Chen[a,e], Mi Jiang[f], Xiao Cheng[f], Jiasong Zhu[a,b] and Qingquan Li[a,b]

[a]MNR Key Laboratory for Geo-Environmental Monitoring of Great Bay Area & Guangdong Key Laboratory of Urban Informatics, Shenzhen University, Shenzhen, China; [b]College of Civil and Transportation Engineering, Shenzhen University, Shenzhen, China; [c]Shenzhen Research Institute, The Hong Kong Polytechnic University, Shenzhen, China; [d]Department of Land Surveying and Geo-Informatics, The Hong Kong Polytechnic University, Hong Kong, China; [e]School of Architecture & Urban Planning, Shenzhen University, Shenzhen, China; [f]School of Geospatial Engineering and Science, Sun Yat-sen University, Zhuhai, China

ABSTRACT

Structural health monitoring of long-span bridges is critical to their safe operation and ensuring efficient daily traffic. Ground-based interferometric radar (GBIR) and inertial vision-based measurement (IVM) can capture linear and point deformation of long-span bridges, respectively. In this paper, we propose a framework to obtain a multi-dimensional dynamic deformation time series by fusing these two datasets with procedures of spatial-temporal alignment, interpolating, established deformation spatial-temporal correlation models, and weighting. To our knowledge, it was experimented on the Xijiang Railway Bridge, located in Guangdong, China, which is the first combination of these two data. Deformations along the vertical and lateral directions were derived when trains crossed the bridge. To validate the effectiveness of the derived results, static leveling sensors and vibrometers were employed on the bridge to obtain instantaneous measurements. The results show that the derived deformation is consistent with these in-situ measurements and the accuracy has improved by 27.4% and 27.0% compared with GBIR and IVM, respectively. The framework combining GBIR and IVM performs well in multi-dimensional dynamic deformation monitoring of long-span bridges and can play an important role in structural health monitoring of similar structures.

ARTICLE HISTORY
Received 29 August 2024
Accepted 24 March 2025

KEYWORDS
Long-span bridge; multi-dimensional dynamic deformation; Ground-based interferometric radar (GBIR); inertial vision-based measurement (IVM); data fusion

1. Introduction

Long-span railway bridges play a crucial role in modern travel and enhance transportation efficiency. However, these vital structures are susceptible to various hazards, such as structure aging, design flaws, load-bearing, and natural disasters like earthquakes and typhoons (Xu and Xia 2011), which can lead to structural defects and potential collapse, which even bring about numerous casualties and significant economic losses. Structure health monitoring (SHM) of long-span bridges is essential to avoid this kind of tragedy.

Deformation monitoring is an important part of SHM, providing insights into the operational and health status of the bridge. It also limits the maximum crossing speed of the bridge (Xia and Zhang 2005). However, comprehensive deformation monitoring is challenging as it requires high sampling frequency and spatial density monitoring. High spatial density cannot be achieved by point-wise monitoring techniques, including robotic total station (RTS) (Psimoulis and Stiros 2013), global navigation satellite system (GNSS) (Xin et al. 2018), vision-based measurement (VM) and contact sensors, such as accelerometer (Sekiya, Kimura, and Miki 2016), level sensing station (Vurpillot et al. 1998) and strain sensor (Castro et al. 2018). Techniques that fulfill high spatial density usually fail to achieve high sampling frequency. These techniques include terrestrial laser scanning (TLS) (Rashidi et al. 2020), close-range terrestrial photogrammetry (Jiang, Jáuregui, and White 2008), spaceborne interferometric synthetic aperture radar (InSAR) (Wang et al. 2024; Zhao et al. 2017), and ground-based interferometric radar (GBIR). Neither of these two types can accomplish high spatial and temporal sampling at the same time.

GBIR is versatile in various applications, such as landslides (Lowry et al. 2013), glaciers (Luzi et al. 2007), mining areas (Hu et al. 2019), buildings (Zhang et al. 2023), and dams (Qiu et al. 2020). Compared with spaceborne InSAR, GBIR is fixed during monitoring with a maximum monitoring frequency of 4000 Hz, and therefore has higher temporal and spatial resolution (Calò et al. 2024; Farneti et al. 2023; Werner et al. 2008). It also offers portability and high accuracy, making it particularly

CONTACT Bochen Zhang bochen.zh@gmail.com

suitable for bridge monitoring. In 2004, the prototype of a high-speed coherent radar for dynamic monitoring of civil engineering structures was conducted (Pieraccini et al. 2004). Since GBIR can only achieve the deformation along the line of sight (LOS) direction, the direction and position of the instrument should be carefully considered in the observing geometry (Huang et al. 2020; Wu et al. 2023; Zhang et al. 2018; Zhang et al. 2016). Many studies have remarked on the impressive high accuracy of up to 5–6 mm of bridge deformation monitoring using GBIR (Zhu et al. 2021). Furthermore, GBIR has been shown to accurately measure deflection changes, natural vibration frequency, and spectrum characteristics of bridges in near-real-time (Long et al. 2022).

Bridge deformation can be caused by various factors, which combinedly lead to multi-dimensional deformation. For instance, wind load can cause lateral deformation, and the self-weight of the bridge cause vertical deformation. Deformation caused by traffic load is complex as it is related to bridge structures, and it can manifest in longitudinal, lateral, and vertical directions. It is challenging to retrieve the multi-dimensional deformation through measurement in one single direction. Some studies have proposed a strategy for multi-dimensional deformation monitoring using monostatic/bistatic interferometric radar techniques (Miccinesi and Pieraccini 2020). The main limitation of this method is the requirement for a sufficiently large spatial baseline between devices (Miccinesi, Beni, and Pieraccini 2021). Some studies have conducted bridge monitoring experiments based on different baselines and provided recommended baseline schemes (Michel and Keller 2021; Talich et al. 2023). But this approach is prohibitively expensive and hardly to be used in wider applications.

To this end, we propose a data fusion model that combines GBIR and inertial vision-based measurement (IVM) data to achieve the multi-dimensional dynamic deformation monitoring of a long-span bridge for the first time. The proposed data fusion framework encompasses spatial-temporal data alignment, spatial interpolation, weighting strategy, and multi-source data fusion. The innovative approach is particularly beneficial for measuring multi-dimensional dynamic deformation based on GBIR and different types of sensors with ultra-high spatial or temporal resolution.

2. Methods and instruments

2.1. Ground-based interferometric radar

The GAMMA portable radar interferometer (GPRI) is a type of real aperture GBIR which is shown in Figure 1. It consists of a transmit antenna and two receiving antennas, an antenna bracket with a GPS antenna, RF electronics assembly, azimuth position, tripod, instrument computer, and a battery pack. The technical parameters of GPRI are listed in Table 1. GPRI is versatile in deformation monitoring, with two main monitoring modes, namely, the rotated azimuth scanning (RAS) mode and fixed azimuth scanning (FAS) mode. In RAS mode, GBIR can monitor the panoramic viewing by rotating the antenna through an azimuth positioner. In this mode, the time to obtain an interferometric image is tens of seconds to minutes. RAS is suitable for short-term or long-term monitoring of the entire bridge and its surrounding environment. In FAS mode, high-frequency dynamic deformation of targets in the imaging direction will be monitored, with the antenna direction fixed. 1D interference time series images in linear areas are obtained within the monitoring period. The sampling frequency of the FAS mode is up to 4000 Hz. FAS is suitable for capturing the dynamic deformation of linear structures, such as long-span bridges.

Figure 1. The GAMMA GPRI II instrument.

Table 1. Technical characteristics of GBIR.

Parameter	Value
Radar type	FMCW
Central frequency	17.2 GHz（Ku-band）
Bandwidth	200 MHz
Polarization	VV
Beam width	0.4×35 °
Measurement range	5–10000 m
Spatial resolution (range×azimuth)	0.75×6.8 m @ 1 km
Displacement accuracy	less than 1 mm @ 1 km
Maximum sampling frequency	4000 Hz
Radar image product	1D or 2D
Time reference	GPS time

2.2. Inertial vision-based measurement

The inertial camera encompasses a high-frequency infrared camera and a high-precision three-axis gyroscope inertial sensor, as shown in Figure 2. The inertial camera is designed as a rectangular box with two cameras mounted on two sides. This inertial camera has a monitoring frequency of 10–30 Hz and can monitor the dynamic deformation of target points. The high-precision three-axis gyroscope inertial sensor records changes in the camera's position and pose, which can be further used to correct camera vibration errors (Shah et al. 2022).

Adding inertial sensors to the real-time vision-based deformation measurement overcomes error propagation by increasing monitoring distance and bridge vibrations. The inertial camera system was deployed in a multi-camera serial connection mode and installed along the axis of the long-span bridge. Multiple targets were arranged between two adjacent inertial cameras at the axis. Images with targets were collected by cameras, and the vertical and horizontal coordinates of target pixels in the images were extracted. Meanwhile, errors caused by camera vibration were corrected using position and pose data acquired through inertial sensors. The vertical and horizontal deformations of each measuring point can be then calculated using different deformation models. Detailed data processing algorithms can be found in (Li et al. 2023).

3. GBIR and IVM data fusion

Due to the different installed positions and viewing geometry, the GBIR and IVM measure bridge deformation in different directions. The former captures the LOS deformation in the GBIR LOS plane, while the latter measures vertical and lateral deformation in the IVM observation plane. As shown in Figure 3, the three measured deformation components are not in the same plane, thus, the three-dimensional dynamic deformation along the longitudinal, lateral, and vertical directions of the main span can be retrieved by fusing these different measurements. To this end, we proposed a data fusion algorithm composed of spatial-temporal data alignment, spatial model establishment, and multi-source data fusion with a new weight strategy. The flow chart of the algorithm is shown in Figure 4. The fusion model is expressed as Equation (1):

$$\begin{aligned} \boldsymbol{Z}_t &= \begin{bmatrix} d_{GBIR_{los}} \\ d_{IVM_{ver}} \\ d_{IVM_{lat}} \end{bmatrix} \\ &= \begin{bmatrix} \cos\theta & \sin\theta cos\gamma & \sin\theta sin\gamma \\ 1 & 0 & 0 \\ 0 & 1 & 0 \end{bmatrix} \begin{bmatrix} \hat{d}_{ver} \\ \hat{d}_{lat} \\ \hat{d}_{lon} \end{bmatrix} \end{aligned} \quad (1)$$

where $\boldsymbol{Z}_t$ is the observation matrix at time t. $d_{GBIR_{los}}$, $d_{IVM_{ver}}$, $d_{IVM_{lat}}$ represent the LOS deformation measured by GBIR, the vertical and lateral deformations measured by IVM, respectively. θ represents the incident angle between the LOS and the horizontal plane,

Figure 2. The inertial camera instrument is set up inside the bridge.

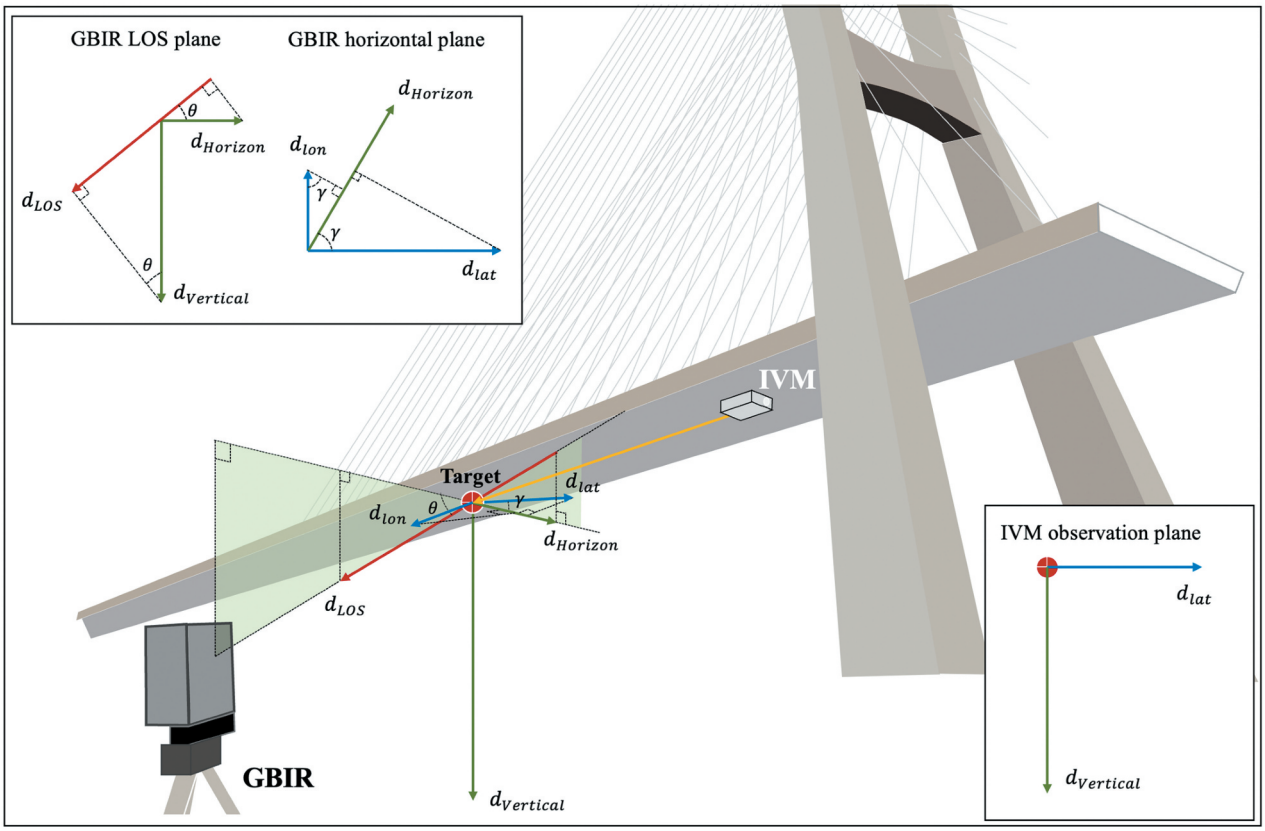

Figure 3. The observation geometry of the bridge with GBIR and IVM.

and γ denotes the angle between the GBIR and IVM planes. $\hat{d}_{ver}$, $\hat{d}_{lat}$, $\hat{d}_{lon}$ represent three deformation components derived by using the fusion model.

3.1. Spatial-temporal data alignment

To fuse the bridge deformation measured in the independent GBIR and IVM planes, a common coordinate needs to be established for spatial alignment. The coordinate origin (x_0, y_0, z_0) is chosen to be the point on the near end of the main span. The x-axis is parallel to the traffic direction. The y-axis points away from the GBIR sensor whose location is (x_G, y_G, z_G), and the z-axis points vertically downward. Using Inte as the interval of the x-axis, the x-coordinate for each monitoring point along the main span of the bridge is obtained.

$$Inte(s) = \left(\tan\gamma_s - \tan\gamma_{s-1}\right)\left(y_G - y_0\right) \tag{2}$$

$$\gamma_s = \arccos\frac{y_G - y_0}{\sqrt{\left(x_s - x_0\right)^2 + \left(y_s - y_0\right)^2}} \tag{3}$$

where $s = 1, 2, \cdots N$ represents the index of the target point. γ_s represents the azimuth angle of s-th monitoring point (x_s, y_s, z_s) and $\gamma_0 = 0$.

Subsequently, measurements in the GBIR and IVM planes should be transformed into a common coordinate. Cameras and sensors were sparsely deployed along the axis of the bridge. Their coordinates are determined based on their relative distances. Their distances from GBIR were calculated with the image acquired in RAS mode with a range resolution of 0.75 m per pixel. Deformation monitoring was performed in FAS mode with the same location of GBIR as the RAS mode. GBIR data can be registered to the common coordinate system by matching the GBIR position to the origin of the coordinate.

GBIR operates using a GPS clock set to Coordinated Universal Time (UTC) at 100 MHz, while IVM uses a Network Time Protocol (NTP) clock set to Beijing Time at 100 Hz. The clock error is corrected, and the temporal alignment between the two systems is straightforward with the removal of the 8-hour difference. Both GBIR and IVM have a sampling frequency exceeding 10 Hz, which is the minimum standard for dynamic deformation monitoring, so we can obtain data with matching sampling frequency through simple time interpolation without affecting the quality of dynamic deformation monitoring.

3.2. Spatial model establishing

IVM has a sparse spatial distribution and cannot achieve the same spatial density as GBIR. Therefore, it is necessary to interpolate the IVM to match the spatial density of GBIR. The Kriging interpolation has been widely used for spatial interpolation (Oliver and

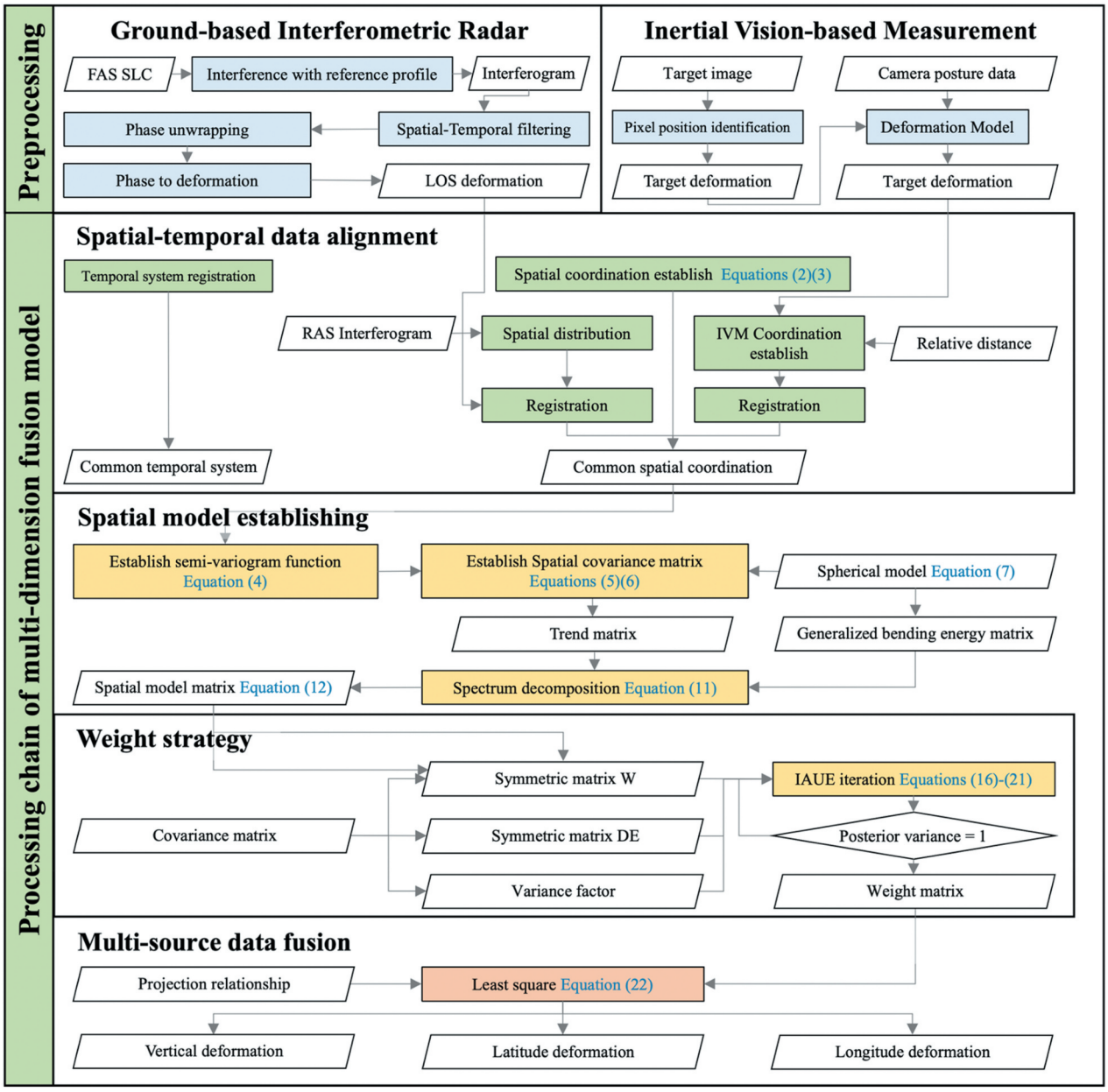

Figure 4. Flow chart of multi-dimensional dynamic deformation fusion algorithm.

Webster 2014). Its fundamental assumption is that closer sampled points tend to exhibit greater similarity (Aryafar, Khosravi, and Karami 2020), relying on variogram theory and structural analysis (Lu et al. 2020). The robust semi-variogram function (Cressie and Hawkins 1980; Lebrenz and Bárdossy 2017) is selected here to describe the spatial characteristics of GBIR and IVM because of the accuracy difference:

$$r(d)=\frac{\left(\frac{1}{m(t,d)}\sum_{t=1}^{ML}\sum_{s=1}^{m(t,d)}\left(D_t(x_s)-D_t(x_s+d)\right)^{\frac{1}{2}}\right)^4}{2\times\left(0.457+\frac{0.494}{\sum_{t=1}^{ML}(t,d)}\right)} \tag{4}$$

where $m(t,d)$ is the number of points with lag distance d and time t, ML is the number of monitoring time of resampling data, $D_t(x_s)$ is the deformation data of one of the sensors at time t and x_s is the distance from monitoring point (x_s,y_s,z_s) to reference point (x_0,y_0,z_0).

A spatial covariance matrix based on a spherical model is employed here to quantify the spatial correlation among points on the bridge:

$$D(i,j)=\sigma(x_i,x_j) \tag{5}$$

$$\sigma(x_i,x_j)=C_0+C_1-\theta(x_i-x_j) \tag{6}$$

$$\theta(d)=\begin{cases}0 & d=0\\ C_0+C_1\left(\frac{3d}{2a}-\frac{d^3}{2a^3}\right) & 0\le a\\ C_0+C_1 & d>a\end{cases} \tag{7}$$

where D denotes the spatial covariance matrix and $D(i,j)$ denotes the i-th row and jth column

element. $\sigma(x_i, x_j)$ denotes the spatial covariance function. $\| x_i - x_j \|$ represents the distance between the point i and point j. C_0, C_1, and a represent the nugget value, partial sill value, and the range of the spherical model, respectively. The fitting of the spatial covariance function can also reduce the impact of the outlier values.

The location of monitoring points is known and the distance between known points and unknown points can be calculated. Substituting the distance into spatial covariance Equation (6), the spatial interpolate weight vector $\boldsymbol{V}$ of one of the unknown points can be obtained:

$$\boldsymbol{V} = \begin{bmatrix} \nu_1 \\ \vdots \\ \nu_n \\ \lambda \end{bmatrix} = \begin{bmatrix} \sigma_{11} & \cdots & \sigma_{1n} \\ \vdots & \ddots & \vdots \\ \sigma_{n1} & \cdots & \sigma_{nn} \\ 1 & 1 & 0 \end{bmatrix}^{-1} \begin{bmatrix} \sigma_{10} \\ \vdots \\ \sigma_{n0} \\ 1 \end{bmatrix} \tag{8}$$

The interpolation values of unmonitored points are calculated based on the data that points are monitored and the weight vector:

$$\hat{d}_i(t, s) = \boldsymbol{V} \times d_i \tag{9}$$

where $\hat{d}_1$, $\hat{d}_2$ represent interpolated values of vertical, lateral respectively, at point (x_s, y_s, z_s) on the bridge at time t of the IVM data.

The spatial model matrix describes the spatial distribution of monitoring data. After the spatial covariance function is determined, the generalized bending energy matrix is calculated as follows (Mardia et al. 1998):

$$\begin{cases} \mathbf{A} = \left(F^{\mathrm{T}} D^{-1} F\right) F^{\mathrm{T}} D^{-1} \\ \mathbf{B} = D^{-1} - D^{-1} F A \end{cases} \tag{10}$$

where $(*)^{\mathrm{T}}$ is the transpose symbol; $\boldsymbol{A}$ represents the trend matrix, $\boldsymbol{B}$ represents the generalized bending energy matrix describing the degree of spatial variation, and F is the spatial trend field matrix. Due to the large amount of GBIR and IVM monitoring data, spectrum decomposition is performed on $\boldsymbol{B}$ to reduce the dimension:

$$\begin{cases} \mathbf{B} = UDU^{\mathrm{T}} \\ \mathbf{B}u_i = d_i u_i \end{cases} \tag{11}$$

where u_i and d_i are the eigenvectors and eigenvalues of $\boldsymbol{B}$, respectively. $U = [u_1, u_2, \cdots, u_n]$ and $D = [d_1, d_2, \cdots, d_n]$.

The spatial model matrix H consists of three spatial model components from GBIR H^{GBIR}, the vertical direction of IVM $H^{IVM_{ver}}$, and the lateral direction of IVM $H^{IVM_{lat}}$ and shown as in Equation (12).

$$H = \left[H^{\mathrm{GBIR}}, H^{\mathrm{IVM_{ver}}}, H^{\mathrm{IVM_{lat}}}\right]^{\mathrm{T}} \tag{12}$$

$$H^{\mathrm{GBIR}} = \left[h_{\mathrm{GBIR}}(S_1), h_{\mathrm{GBIR}}(S_2), \cdots, h_{\mathrm{GBIR}}(S_n)\right]^{\mathrm{T}} \tag{13}$$

$$h(s) = \left[F(s)^{\mathrm{T}}, d_3 \sigma(s)^{\mathrm{T}} u_3, \cdots, d_n \sigma(s)^{\mathrm{T}} u_n\right] \tag{14}$$

3.2. Spatial model establishing

Helmert variance component estimation (HVCE) has been used to estimate the variance components of InSAR and MAI for ascending and descending orbits (Liu et al. 2017). The disadvantage of HVCE is that it is prone to negative variance components and may be difficult to converge (Teunissen and Amiri-Simkooei 2008). The presence of negative variance components may lead to a nonpositive definite covariance matrix, rendering it physically uninterpretable. This limitation is addressed by the Iterative Almost Unbiased Estimation (IAUE) method.

IAUE (Hsu 1999) has been used to estimate the variance components of InSAR and GNSS (Ji et al. 2020) and proved to be a superior method compared with least-squares (LS) and weight least-squares (WLS) (D. W. Qiu et al. 2023). Instead of estimating the variance component σ_i^2 directly, IAUE estimates the variance factor f_i by multiple iterations. The almost unbiased estimated variance component is obtained by multiplying the initial estimate $\hat{\sigma}_i^2$ and variance factor f_i:

$$\sigma_i^2 = f_i \hat{\sigma}_i^2, i = 1, 2, \cdots k \tag{15}$$

where σ_1^2, σ_2^2, σ_3^2 are the true variance of GBIR observation, and the vertical and lateral observation of IVM, respectively. The covariance matrix $\boldsymbol{R}$ of the observation vector $\boldsymbol{Z_t}$ can be represented as

$$\boldsymbol{R} = \sum_{i=1}^{3} f_i B_i = \begin{bmatrix} f_1 \hat{b}_1 & 0 & 0 \\ 0 & f_2 \hat{b}_2 & 0 \\ 0 & 0 & f_3 \hat{b}_3 \end{bmatrix} \tag{16}$$

where $B_i = \hat{\sigma}_i^2 R_i$ and $b_i = \hat{\sigma}_i^2 I_i$ ($i = 1, 2, 3$ and I_i is a unit matrix) is a diagonal matrix associated with data group i. The variance factor is calculated with (Lucas 1985):

$$f_i = \frac{{Z_t}^{\mathrm{T}} W B_i W Z_t}{tr(W B_i)}, i = 1, 2, 3 \tag{17}$$

$$\boldsymbol{W} = P - PH\left(H^{\mathrm{T}} PH\right)^{-1} H^{\mathrm{T}} P \tag{18}$$

where $tr(*)$ represents the sum of the diagonal elements of the matrix, and $P = R^{-1}$. To facilitate the calculation of the variance factor, the approximated expression of Equation (19) is as follows:

$$f_i = \frac{[de_i]}{{Z_t}^{\mathrm{T}} W B_i W Z_t}, i = 1, 2, 3 \tag{19}$$

$$\boldsymbol{DE} = I - H\left(H^{\mathrm{T}}PH\right)^{-1}H^{\mathrm{T}}P \tag{20}$$

where $[de_i]$ represents the sum of all diagonal elements in the ith group of matrixes $\boldsymbol{DE}$. The iteration stops until posterior variance converges to 1:

$$\hat{m} = \frac{1}{N-p}\sum_{t=1}^{2}[de_i]f_i \tag{21}$$

where N is the number of GBIR because its monitoring point coincides with that of IVM; p is the number of monitoring sensors and $p = 3$ for the three-dimensional deformation model. IAUE method avoids negative variance components and has a good performance in variance components estimation of GBIR and IVM.

3.4. Multi-source data fusion

Once these two types of measurements are aligned spatially and temporally, data fusion can then be achieved through the LS solution of Equation (1) with the determined weight strategy, as expressed in Equation (22).

$$\hat{d} = \left(Pr^{\mathrm{T}}PPr\right)^{-1}Pr^{\mathrm{T}}PZ_t \tag{22}$$

where $\hat{d}$ represents the result vector including deformation in the vertical, lateral, and longitudinal directions in the fusion model result; $\boldsymbol{Pr}$ is the projection relationship of each deformation vector. $\boldsymbol{P}$ is the weight matrix obtained in the weight strategy part and P_1, P_2, P_3 represent the weight matrix corresponding to deformation vectors.

$$\boldsymbol{Pr} = \begin{bmatrix} \cos\theta & \sin\theta\cos\gamma & \sin\theta\sin\gamma \\ 1 & 0 & 0 \\ 0 & 1 & 0 \end{bmatrix} \tag{23}$$

$$\boldsymbol{P} = \begin{bmatrix} P_1 & 0 & 0 \\ 0 & P_2 & 0 \\ 0 & 0 & P_3 \end{bmatrix} = \begin{bmatrix} f_1\hat{b}_1 & 0 & 0 \\ 0 & f_2\hat{b}_2 & 0 \\ 0 & 0 & f_3\hat{b}_3 \end{bmatrix}^{-1} \tag{24}$$

4. Study area and data collection

The Xijiang Railway Bridge crosses the boundary between Jiangmen and Foshan cities after the divergence of the Haizhou channel from the Xijiang River. Xijiang Bridge consists of two bridges, a highway bridge and a railway one. The bridge is a twin-tower, double-cable plane steel box mixed-girder cable-stayed bridge with a total length of 1,117.5 m and a main span of 600 m. As a part of the Nansha Port Railway, which traverses Jiangmen, Zhongshan, Foshan, and Guangzhou, the Xijiang Bridge plays a crucial role in railway transportation within the Greater Bay Area.

Field work for monitoring the deformation of the Xijiang Bridge was conducted from October 24 to 26 October 2022. GBIR and IVM were used to measure its deformations. GBIR was deployed on the land opposite the bridge, nearly parallel to the bridge tower to avoid signal overlap. Extra sensors, such as static leveling and vibrometers are installed on the bridge for cross-validation. The installation locations of the sensors and monitoring area of GBIR are shown in Figure 5.

FAS mode was used with a scanning distance of 50–1300 m including the whole main span. 68 images with each monitored for 1800 s were obtained with 500 Hz sampling frequency. To improve the SNR of the images, an azimuth multi-look factor of 20 was used and it is still high enough for the frequency to express the dynamic deformation characteristics of the bridge.

The inertial cameras and measurement targets were welded into the bridge box girder through the steel frame (Talich et al. 2023). Among the 5 cameras, 2 were fixed at the bridge towers and regarded to be stable points with no deformation, while the others were set at the one-fourth, middle, and three-fourth positions of the main span, respectively. Twelve targets were evenly distributed at the remaining locations on the main span and adjacent IVMs had the same distance to each other.

5. Results

5.1. Deformation result of GBIR and IVM

During the monitoring period, 8 trains were passing through the Xijiang Bridge, and some of the corresponding interference images are shown in Figure 6.

The LOS deformation and its temporal change acquired by GBIR can form images as shown in Figure 6. Columns from left-to-right represent the monitoring points from the near range to the far range of the GBIR. Rows from top-to-bottom arrange the measured LOS deformation in chronological order. The dense fringes crossing the columns of images in Figure 6 are mainly caused by the deformation of the bridge deck, accompanied by slight atmospheric effects. The sparse vertical lines on the right side of the images are caused by the piers which do not belong to the main span as the monitoring line cannot cover the deck with curvature in the vertical direction. In Figure 6a,b, deformation occurs from the up-left to down-right, indicating the passing of a train through the bridge from the near end to the far end. Conversely, in Figure 6c,d, the deformation pattern is from up-right to down-left, meaning that a train moving from the far end to the near end. Both above situations occurred sequentially in the Figure 6e,f.

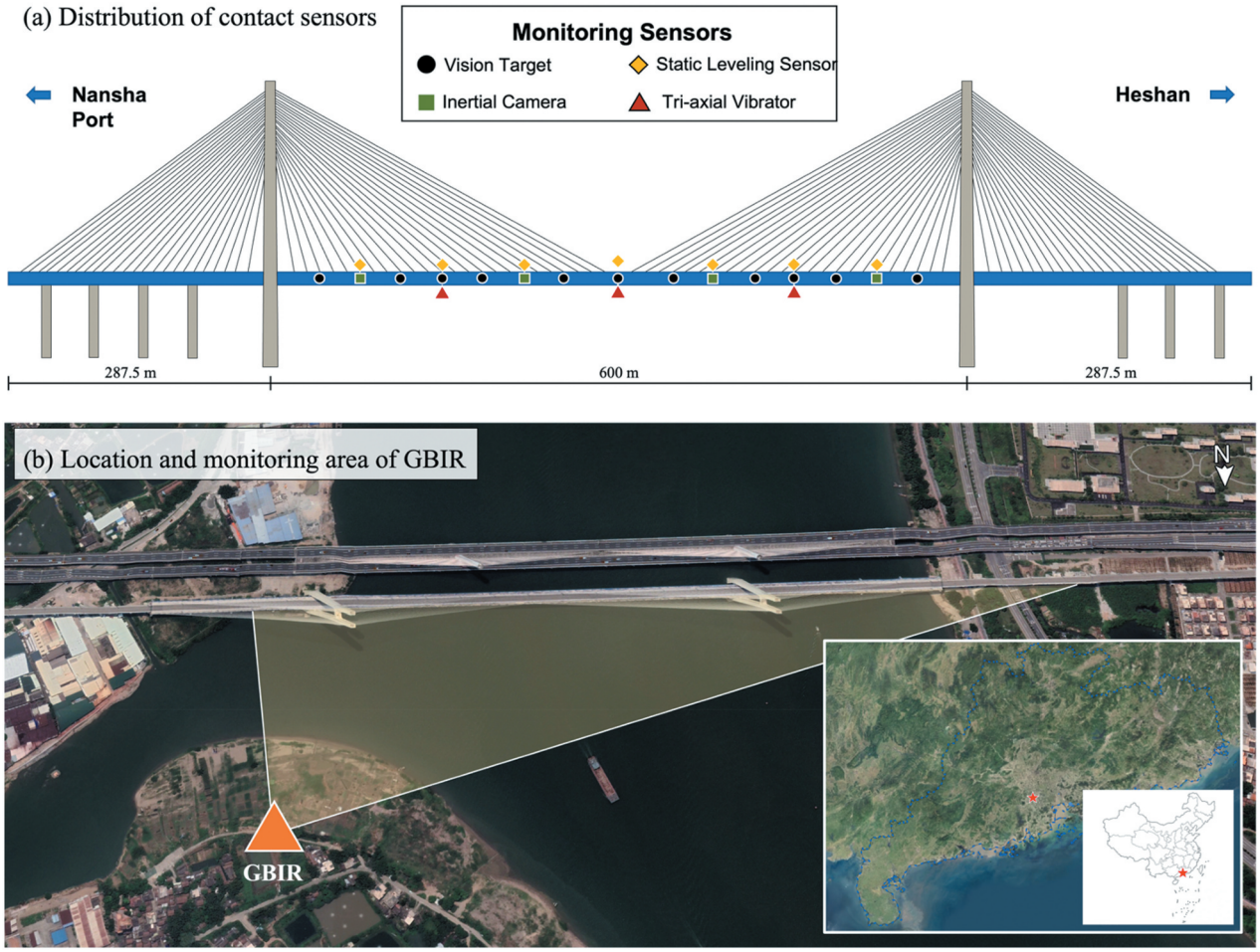

Figure 5. The distribution and monitoring area of GBIR, IVM, static leveling sensor, and tri-axial vibrator.

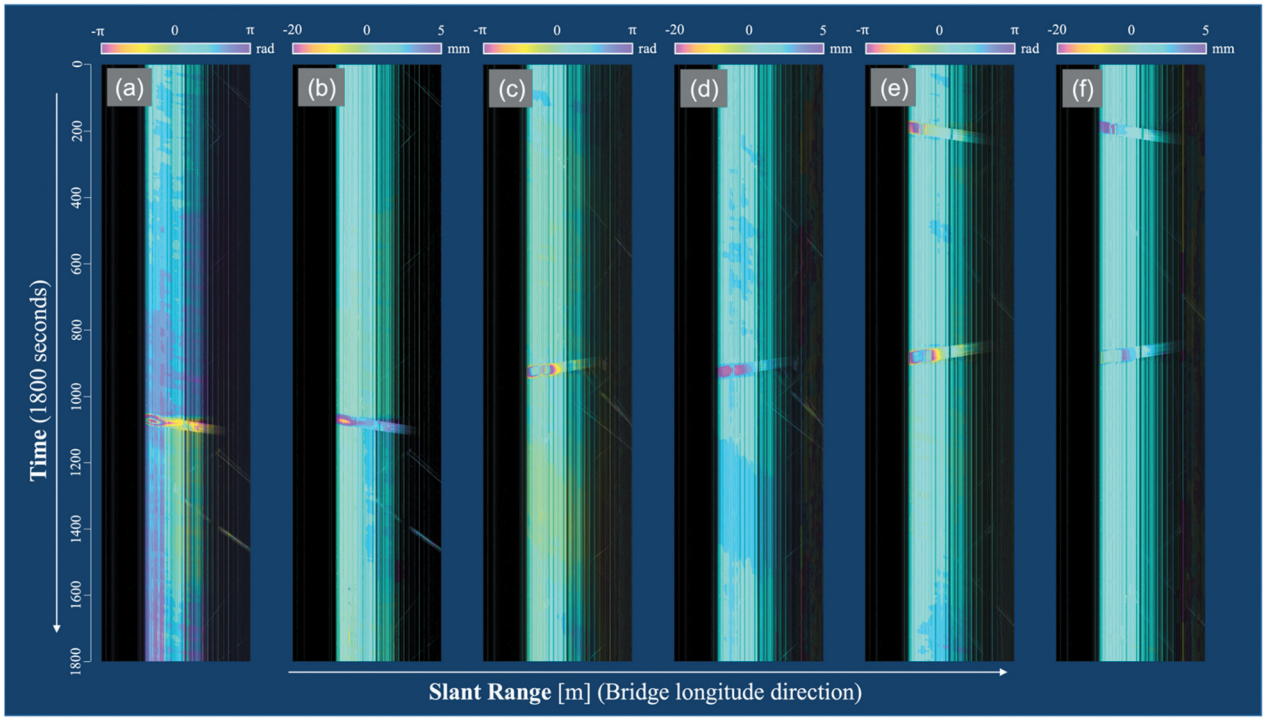

Figure 6. The results of GBIR on different acquisition times.

The time that the train entered and completely left the main span part can be extracted from the interferogram. The train length can be estimated through photos, and the train speed can be calculated. As shown in Figure 6a, the train entered the main span of Xijiang Bridge at about 18:15:02.44 and left at about 18:15:56.40. The length of the main span is 600 m and the length of the train is about 400 m so the average speed of the train can be calculated to be approximately 66.4 km/h.

We choose the middle position and positions at one-fourth and one-eighth of the bridge starting from the near range to obtain the temporal profiles, as shown in Figure 7a. The time points at which the lines reach the maximum values from the side to the middle follow sequence, and the maximum deformation values gradually increase, reaching 16.1 mm near the middle position. The temporal lines do not form completely parabolic shapes, possibly because the LOS deformation consists of vertical and horizontal components.

The time when the train got on the bridge and reached one-eighth, one-fourth, and middle positions was selected to obtain the spatial profiles, as shown in Figure 7b. The position of maximum deformation shifts toward the middle of the bridge as the train moves, and the maximum values gradually increase as the train approaches the middle of the bridge.

The results of IVM are time series deformations of 15 monitoring points in the vertical direction. We select the same positions and time points as GBIR to obtain temporal and spatial profiles, as depicted in Figure 8. The profiles of IVM resemble those of GBIR. The maximum deformation occurred near the middle position of the bridge, reaching 245.7 mm. The differences between GBIR and IVM results can be explained by different observation directions. The monitoring incident angle of GBIR ranges between 88 and 89.5 degrees, resulting in a coefficient ranging from 1/28 to 1/115 when projecting from the vertical direction to the LOS direction, implying that the differences are reasonable.

5.2. Multi-dimensional deformation results

GBIR provides deformation along LOS, which can be decomposed along the three axes of the common coordinate. However, IVM provides deformations in the vertical directions, lacking lateral components. In this case, the model in Equation (1) is degraded into a two-dimensional dynamic deformation model with ignorance of lateral parameters in Equations (1), (12), (16), (23), and (24), assuming no deformation in the direction of train travel. We obtain the deformation results in the vertical and lateral directions through the proposed fusion algorithm and the fusion results are shown in Figure 9. The deformation fringe of the fusion deformation time series images in two directions are both similar to the LOS deformation result of GBIR. This occurs in the vertical direction due to the train load, while the lateral deformation may be attributed to the load acting on only one side of the bridge. The maximum vertical deformation of the fusion model is 211.3 mm, and the maximum lateral deformation is 123.4 mm.

We also select the middle position and positions at one-fourth and one-eighth of the bridge starting from the near range to obtain spatial and temporal profiles, as shown in Figure 10. The profiles of the fusion results are consistent with the single sensor deformation profiles and are closer to a parabola. This may be caused by the decomposition of the LOS deformation into vertical and lateral directions.

The Fourier spectra comparison results are shown in Figure 11 and the vertical and lateral results have similar frequency distributions. When there are no passing trains, the bridge exhibits vibration frequencies at 1/4 and 1/2 of its natural frequency, corresponding to 0.008 Hz and 0.975 Hz, respectively. The 0.975 Hz signal likely results from the bridge's load-induced deformation, while the 0.008 hz signal may be attributed to wind loads.

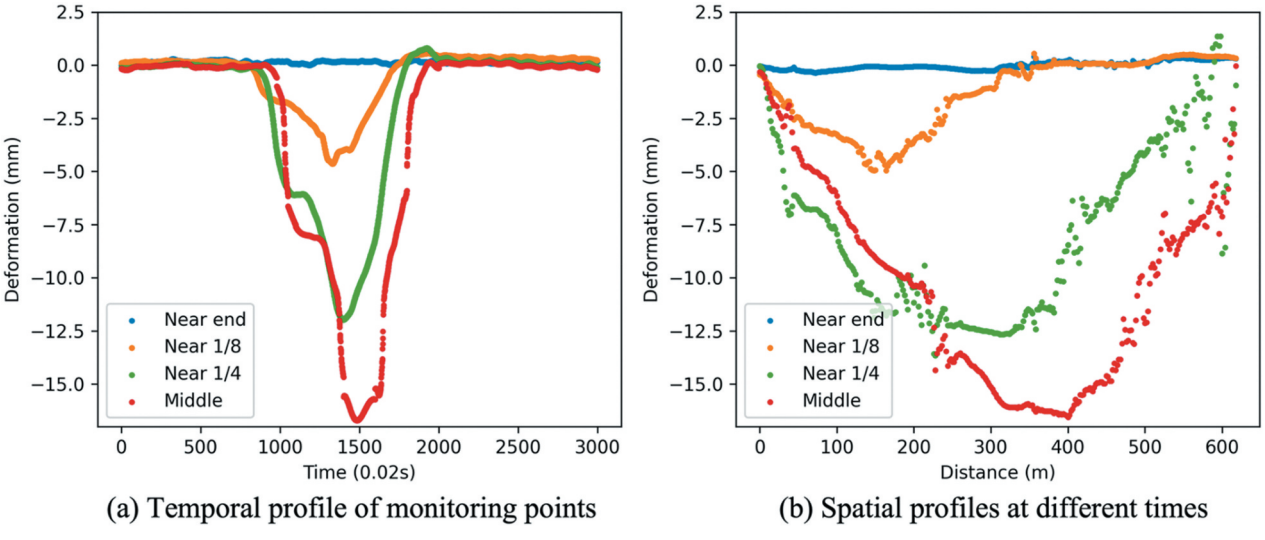

(a) Temporal profile of monitoring points (b) Spatial profiles at different times

Figure 7. The spatial and temporal profiles of LOS direction deformation from GBIR.

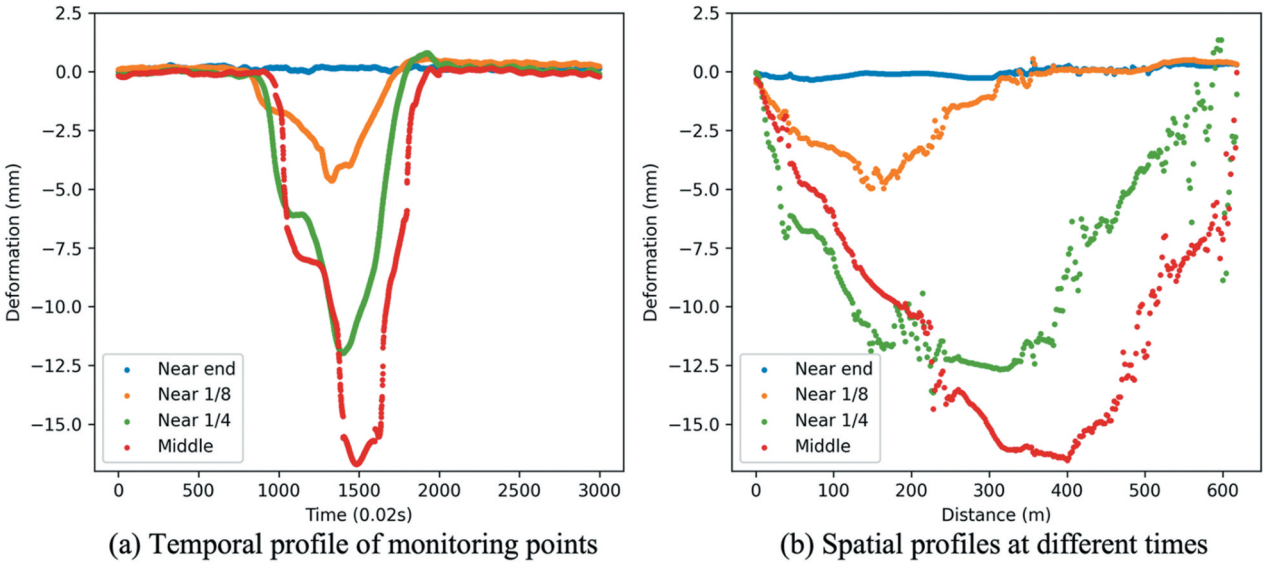

Figure 8. The spatial and temporal profiles of vertical deformation from IVM.

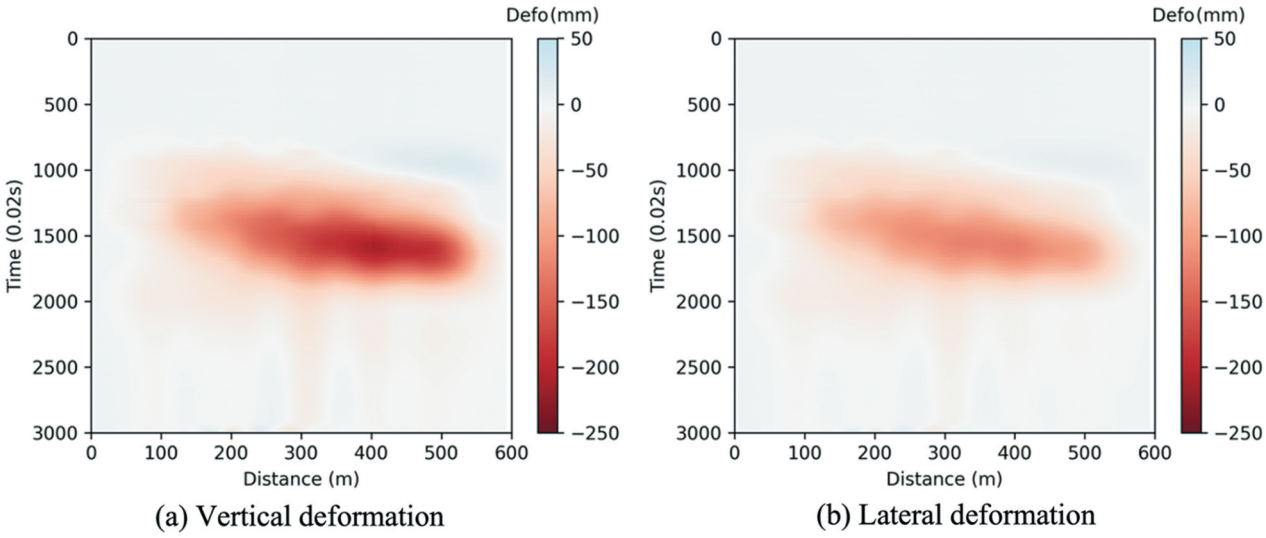

Figure 9. Two-dimensional deformation results of xijiang bridge.

When the train passes over the bridge, additional vibration frequencies emerge, including 0.008, 0.975, 1.998, and 3.918 Hz. Among these, 0.975 Hz still represents the bridge's self-load signal, while 1.998 and 3.918 Hz correspond to the train-induced load signals. The 0.008 Hz frequency may arise from low-frequency effects caused by the train passing over the bridge. The frequency domain results show that the framework proposed also can obtain high-frequency deformation signals of bridges.

6. Discussion

6.1. Validation

Various types of contact sensors were installed on the Xijiang Bridge, and static leveling sensors and vibrometers were used for data verification. Figure 5a demonstrates the 7 static leveling sensors deployed on the one-eighth to the seven-eighth position of the bridge, with 1 Hz monitoring frequency. The vertical deformations at these 7 points were used to validate vertical deformations. Additionally, 3 tri-axial vibrometers with 20 Hz monitoring frequency were deployed to obtain 3D point deformations at one-fourth and middle of the bridge, which were used to validate the fusion result.

The time series profiles of the fused results are plotted in Figure 12 with corresponding results from static leveling and vibrometers. The large difference between the fusion profiles and the vibrator profiles is reasonable as the vibrator is an accelerometer calculating deformation through integration which can cause data to drift. Generally, the results obtained from redundant

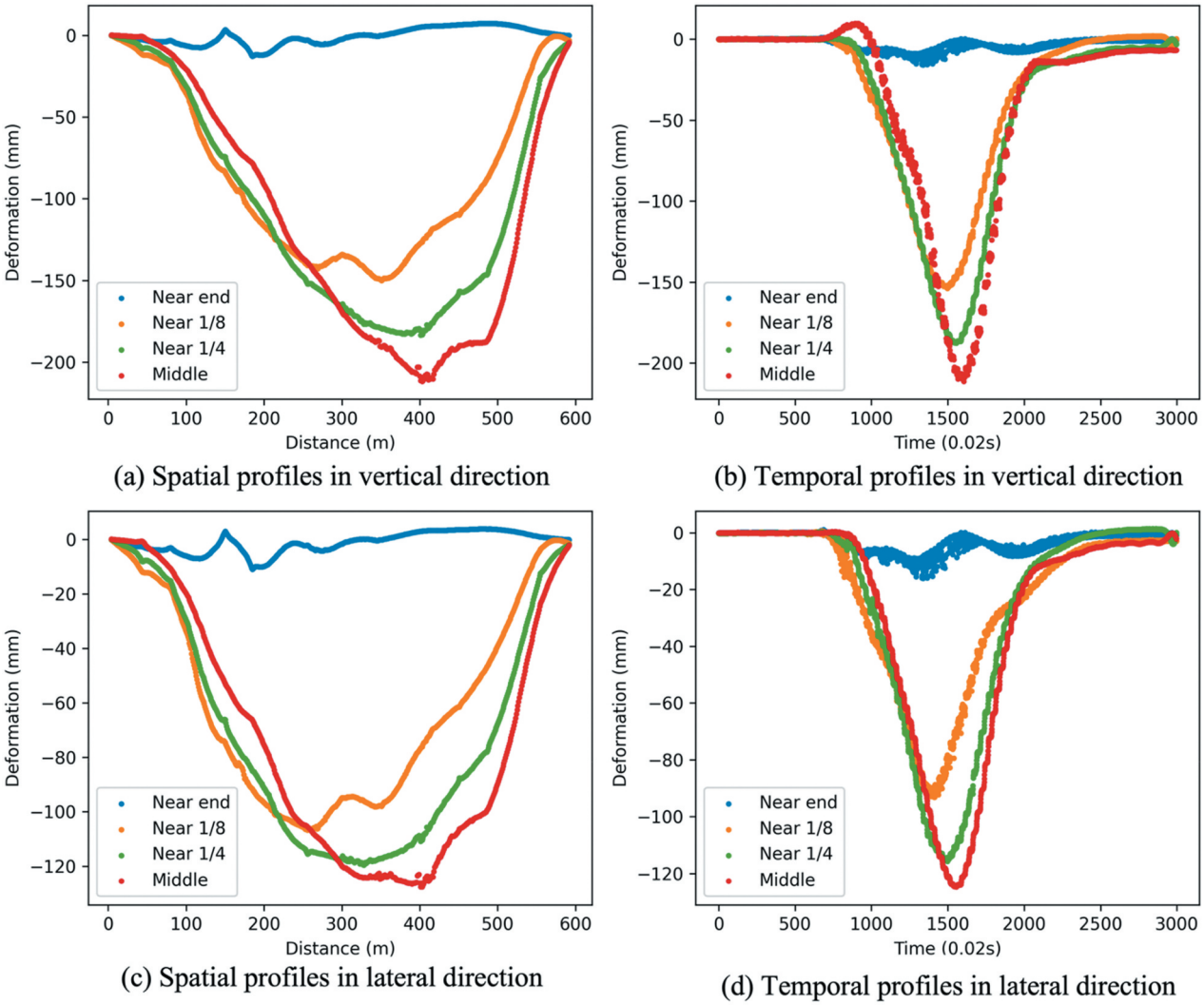

Figure 10. The spatial and temporal profiles of two-dimensional deformation results.

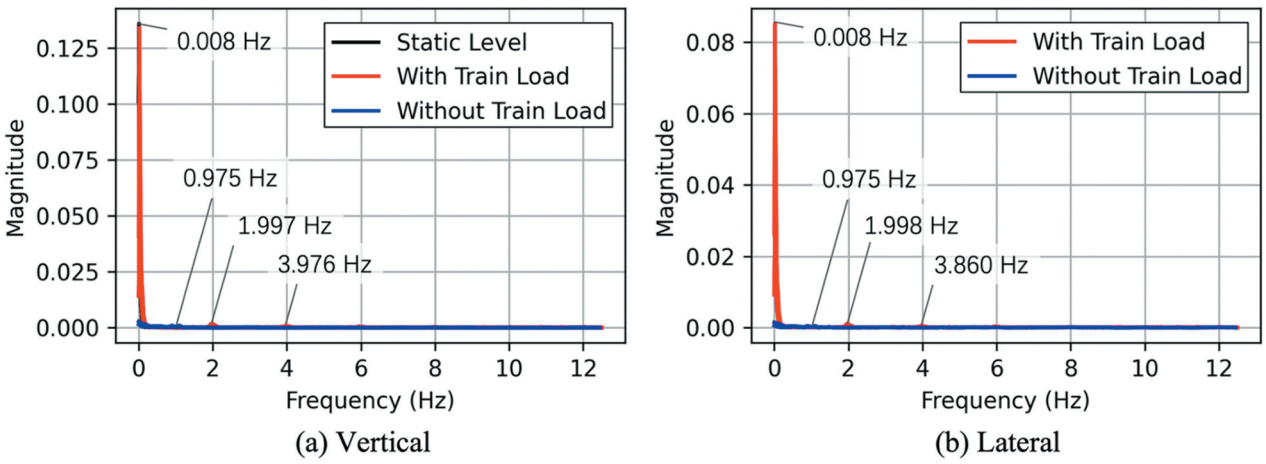

Figure 11. Comparison among the Fourier spectra obtained for the vertical and lateral direction on the bridge with and without train load.

observations are more reliable. In the lateral direction, the difference may come from the fact that vibrometers did not capture the lifting of the bridge deck induced by the train's initial entry onto the bridge.

The mutual exclusion (ME) ε is used as a difference index between the fusion model and sensor data because the results of static leveling and vibrator are not the true values of the bridge deformation.

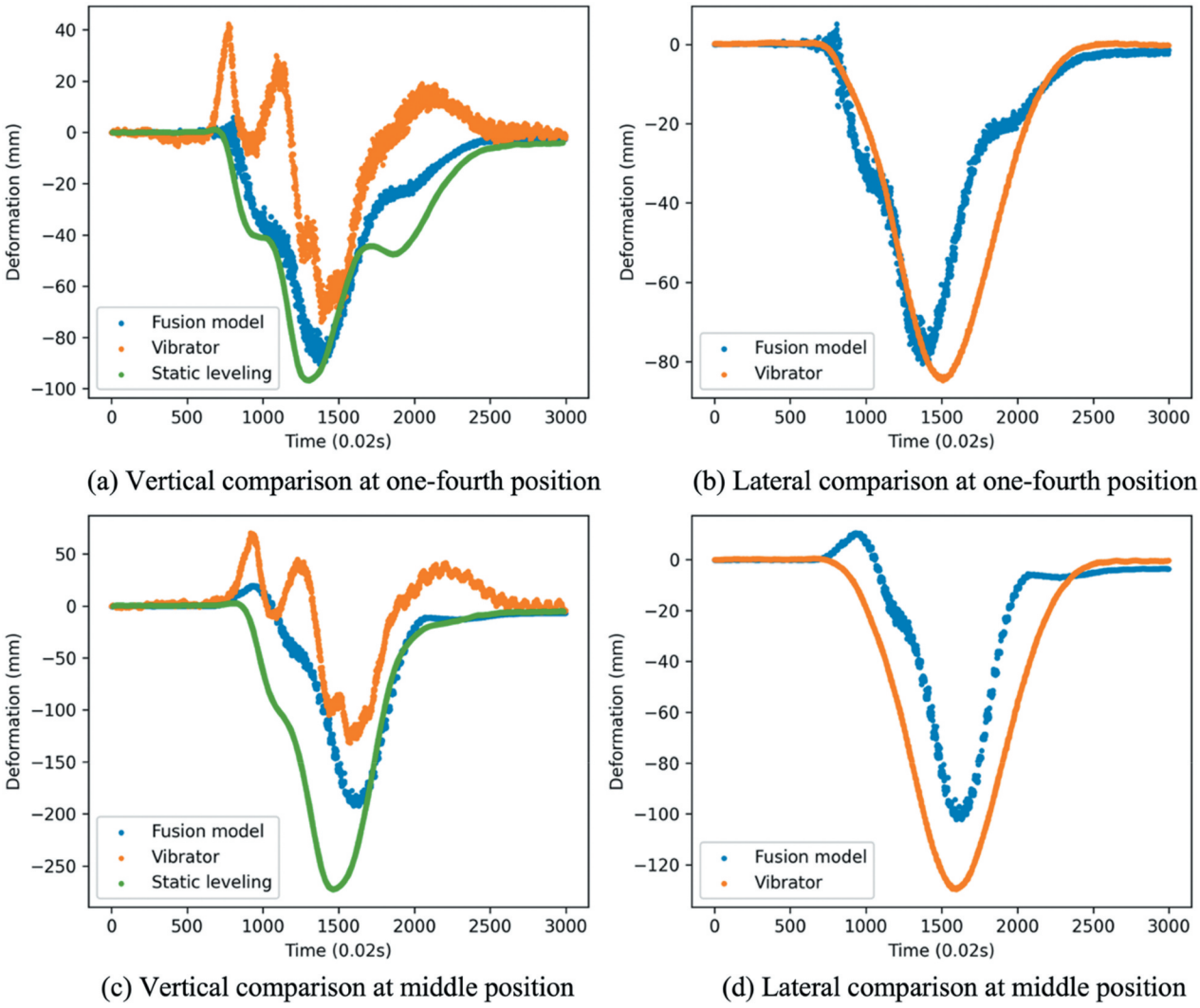

Figure 12. Comparisons of temporal profiles between fusion model with static leveling and tri-axial vibrator.

Table 2. Local mutual exclusion between the results and sensors.

Data	Direction	Mutual Exclusion (mm)
IVM – Static leveling	Vertical	37.1
IVM – Tri-axial vibrator	Vertical	35.6
GBIR – Tri-axial vibrator	LOS	37.1
Fusion – Static leveling	Vertical	27.1
Fusion – Tri-axial vibrator	Vertical	28.0
Fusion – Tri-axial vibrator	Lateral	26.7

$$\varepsilon = \sqrt{\frac{1}{T}\sum_{r=1}^{T}(F_r - S_r)^2} \tag{25}$$

where F represents the fusion results and S represents the leveling or vibrator results; T is the total number of profiles and r is the sequence number. Only the positions monitored by both sensors are selected to calculate the difference index.

The mutual exclusion between GBIR, IVM, and fusion model with static leveling and tri-axial vibrator data are listed in Table 2. The mutual exclusion values of GBIR and IVM with vibrator and static leveling are within the range from 35.6 mm to 37.1 mm. The mutual exclusion values between the fusion result and the other two are between 26.7 mm and 28.0 mm, with an average improvement of 27.4% and 27.0% compared with GBIR and IVM measurements, respectively. In the vertical direction, the mutual exclusion values between the fusion result and static leveling and tri-axial vibrator results are reduced by 27.0% and 21.3%, respectively. In the lateral direction, the mutual exclusion value of 26.7 mm implies that the fusion result is also consistent with the vibrator measurement.

The fusion model has a lower mutual exclusion value than GBIR or IVM. The reason is data errors are mitigated by different monitoring data with the weight matrix based on the variance components. The

results of mutual exclusion demonstrate that this fusion algorithm exhibits good error robustness and can obtain high-quality linear multi-dimensional dynamic deformation results.

6.2. Model error analysis

The relationship between observation and true deformation is described in Equation (1). If GBIR and IVM are in an ideal monitoring environment, the three-dimensional fusion model's accuracy is described in Equation (26), where A_{ver}, A_{lat}, and A_{lon} represent the theoretical errors in vertical, lateral, and longitudinal, and $A_{IVM_{ver}}$, $A_{IVM_{lat}}$, and $A_{GBIR_{los}}$ represent the monitoring errors in the vertical and lateral direction in IVM and LOS direction in GBIR, respectively. In the vertical and the lateral direction, errors of the fusion model are equal to IVM sensors, measuring at 0.38 mm (Li et al. 2023). While the error in the longitudinal direction gradually decreases from the near end of the main span to the far end. The corresponding error diagram is shown as the orange profile in Figure 13. The two-dimensional fusion model's accuracy is described in Equation (27). The error in the vertical direction is also equal to IVM sensors and in the lateral direction increases from near to the far end. The corresponding error diagram is shown as the blue profile in Figure 13. The difference in error change between the lateral and longitudinal directions can be attributed to the observation geometry, which is inclined toward the lateral direction. Additionally, the calculated error is influenced by error propagation from other observation directions, resulting in a larger overall error in the longitudinal direction in the 3D model compared to the lateral error in the 2D model.

$$\begin{cases} A_{ver} = A_{IVM_{ver}} \\ A_{lat} = A_{IVM_{lat}} \\ A_{lon} = \sqrt{\left(\frac{A_{GBIR_{los}}}{\sin\theta\sin\gamma}\right)^2 + \left(\frac{A_{IVM_{ver}}\cos\theta}{\sin\theta\sin\gamma}\right)^2 + \left(\frac{A_{IVM_{lat}}\cos\gamma}{\sin\gamma}\right)^2} \end{cases} \tag{26}$$

$$\begin{cases} A_{ver} = A_{IVM_{ver}} \\ A_{lat} = \sqrt{\left(\frac{A_{GBIR_{los}}}{\sin\theta\cos\gamma}\right)^2 + \left(-\frac{A_{IVM_{lat}}\cos\theta}{\sin\theta\cos\gamma}\right)^2} \end{cases} \tag{27}$$

The proposed weight strategy considers the variance of monitoring sensors, assigning greater weights to smaller errors, thereby mitigating errors to a certain extent. The accuracy of the weight strategy relies on the weight coefficient, which typically tends toward 1. Consequently, the accuracy value is similar to that under ideal conditions.

In the Xijiang Bridge monitoring experiment, the weight of GBIR ranges from 0.962 to 0.994, while the weight of IVM remains approximately 0.999 during non-train periods. This discrepancy stems from GBIR's susceptibility to external disturbances such as atmospheric conditions, whereas IVM, being situated inside the bridge, experiences greater stability. During train crossing periods, the weight of GBIR ranges from 0.951 to 0.992, while that of IVM ranges from 0.986 to 0.998. The weight change coefficient of GBIR is generally about 3.56 times that of IVM, resulting in an observation error of GBIR of 1.35 mm. Additionally, the complex surface of the bridge and the influence of train passage on the monitoring signal contribute to monitoring errors. Based on the above analysis, the actual accuracy of the 2D model of the Xijiang Bridge is estimated to be 0.37 mm and 1.33 mm in the vertical and lateral directions, respectively.

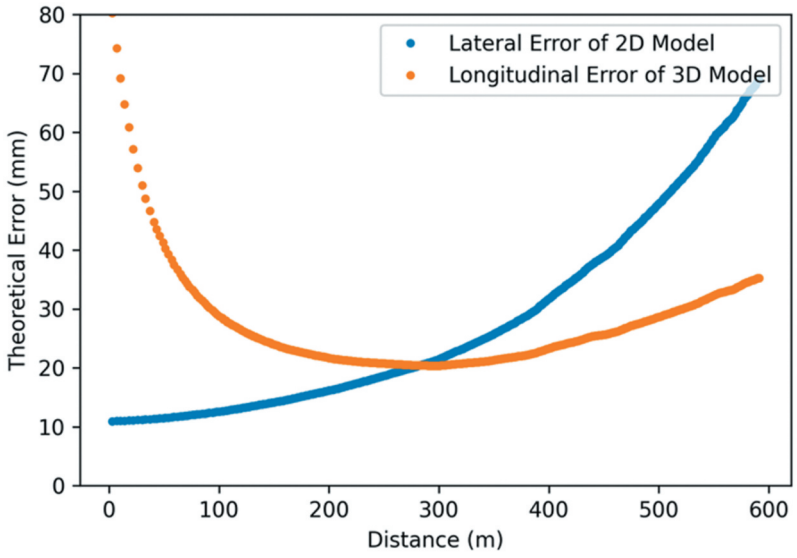

Figure 13. The error diagram of three- and two- dimensional fusion model in an ideal monitoring environment.

6.3. Limitations

In this study, we proposed a multi-source data fusion framework for obtaining the multi-dimensional dynamic deformation of long-span bridges. This framework is applied to fuse GBIR and IVM in the Xijiang Bridge experiment, moreover, it is potentially to be used for fusing other kinds of sensors with multiple monitoring directions and high monitoring frequency, such as global navigation satellite system (GNSS). Numerous single-direction sensors can used to establish a 2D model combined with GBIR data. Typically, high-temporal frequency monitoring techniques suffer errors due to noise and some unavoidable inherent factors. The monitoring of GBIR is also influenced by the uneven bridge structures and monitoring noise. The deformation model fused from redundant observation data demonstrates better robustness to errors from single sensors. Based on the spatial model and weight strategy, our fusion algorithm can alleviate the errors of single sensors to a certain extent, thus improving the accuracy.

As the monitoring experiment is conducted during the bridge trial operation period, the structural health monitoring system on the bridge is unstable. Only deformation data in the vertical direction from IVM is obtained, resulting in the lack of lateral data and the creation of only a 2D fusion model. Therefore, future efforts will concentrate on acquiring complete IVM data to establish a 3D dynamic deformation model. Additionally, installing more precise tri-axis deformation sensors can help reduce errors in result validation.

7. Conclusions

This paper has proposed a data fusion algorithm between GBIR and IVM to establish multi-dimensional dynamic deformation of long-span bridges. The fusion results have been validated with the observations from static leveling and vibrometers on the bridge simultaneously, and they show a relatively consistent agreement with each other. The ME values between fusion data with the other two are between 26.7 mm and 28.0 mm with an average improvement of 27.4% and 27.0% compared with leveling and vibrometer results, respectively. The actual monitoring accuracy of the 2D dynamic deformation model is estimated to be 0.37 mm and 1.33 mm in the vertical and lateral directions, respectively. The results of error analysis demonstrate that this fusion algorithm exhibits high robustness and can obtain high-quality multi-dimensional dynamic deformations. In this study, the lack of longitudinal data resulted in only 2D deformations instead of 3D. Further studies should be carried out to retrieve the 3D dynamic deformation of bridges using the proposed fusion model.

Disclosure statement

No potential conflict of interest was reported by the author(s).

Funding

This work was supported by the National Natural Science Foundation of China [Grant No. 42304014], the Guangdong Basic and Applied Basic Research Foundation [Grant No. 2025A1515012040], Shenzhen Science and Technology Program [Grant No. KCXFZ20240903093000002], the University Grants Council of the Hong Kong Polytechnic University [Grant No. P0045896], and Shenzhen Research Institute, The Hong Kong Polytechnic University [Grant No. C2023A022].

Notes on contributors

Yuhao Liu received the Master's degree from Shenzhen University in 2024. Currently, he is working as a Research Assistant in the Department of Land Surveying and Geo-Informatics at The Hong Kong Polytechnic University, China. His research interests include data processing for ground-based interferometry radar and multi-temporal InSAR.

Songbo Wu is an IEEE member and a Research Assistant Professor in the Department of Land Surveying and Geo-Informatics at The Hong Kong Polytechnic University, China. His research interests include data processing for multi-temporal InSAR, as well as applications related to urban civil infrastructure health monitoring and coastal geological hazards monitoring.

Bochen Zhang is an IEEE senior member and an Associate Professor in the College of Civil and Transportation Engineering, Shenzhen University, China. His research interests include developing algorithms for spaceborne, UAV-borne, and terrestrial radar interferometric data processing, emphasizing geohazards and infrastructure monitoring.

Zhen Peng is currently working toward the Master's degree from Shenzhen University. His research interests include sequential InSAR and error removal algorithms.

Jiayuan Zhang is currently working toward the Master's degree from Shenzhen University. His research interests include multi-temporal InSAR data processing and interpretation.

Chisheng Wang is an Associate Professor at the Department of Urban Informatics, School of Architecture and Urban Planning, Shenzhen University. His research interests include developing algorithms for synthetic aperture radar (SAR) interferometry (InSAR) and light detection and ranging (LiDAR) data processing and applying them in infrastructure and disaster monitoring.

Wei Tu is a Professor at the Department of Urban Informatics, School of Architecture and Urban Planning, Shenzhen University. His research interests include automatics recognition of human activity-mobility from multi-source urban data, trajectory modeling, and analysis and optimization.

Zhipeng Chen is an Assistant Professor in the School of Architecture and Urban planning, Shenzhen University,

China. His current research interests include inertial surveying, integrated navigation, and photogrammetry.

Mi Jiang is an IEEE senior member and a Professor in the School of Surveying and Mapping, Sun Yat-sen University, China. His research interests are in the field of statistical inference with emphasis on synthetic aperture radar processing, as well as the application of the InSAR technique to groundwater parameter inversion.

Xiao Cheng is a Professor and Dean of the School of Geospatial Engineering and Science at Sun Yat-sen University, China. His research interests include polar environment monitoring, modelling and analysis, establish space-borne polar environment monitoring network.

Jiasong Zhu is a Professor with the Department of Transportation Engineering, Shenzhen University, China. His main research interests include smart transportation and transportation infrastructure health monitoring.

Qingquan Li is a member of the Chinese Academy of Engineering and a Professor with Shenzhen University, China. His research areas include 3-D and dynamic data modeling in GIS, location-based service, surveying engineering, integration of GIS, global positioning system and remote sensing, intelligent transportation system, and road surface checking.

ORCID

Songbo Wu http://orcid.org/0000-0003-2118-0963
Bochen Zhang http://orcid.org/0000-0002-2350-2084
Chisheng Wang http://orcid.org/0000-0003-3489-173X
Wei Tu http://orcid.org/0000-0002-0255-4037
Zhipeng Chen http://orcid.org/0000-0001-8537-2409
Mi Jiang http://orcid.org/0000-0003-2459-4619
Xiao Cheng http://orcid.org/0000-0001-6910-6565
Jiasong Zhu http://orcid.org/0000-0001-6177-3363
Qingquan Li http://orcid.org/0000-0002-2438-6046

References

Aryafar, A., V. Khosravi, and S. Karami. 2020. "Groundwater Quality Assessment of Birjand Plain Aquifer Using Kriging Estimation and Sequential Gaussian Simulation Methods." *Environmental Earth Sciences* 79 (10): 1–21. Springer. https://doi.org/10.1007/s12665-020-08905-8.

Calò, M., S. Ruggieri, A. Nettis, and G. Uva. 2024. "A MtinSAR-Based Early Warning System to Appraise Deformations in Simply Supported Concrete Girder Bridges." *Structural Control & Health Monitoring* 2024 (1): 8978782. Wiley Online Library. https://doi.org/10.1155/2024/8978782.

Castro, H. F., V. Correia, N. Pereira, P. Costab, J. Oliveiraa, and S. Lanceros-Méndez. 2018. "Printed Wheatstone Bridge with Embedded Polymer Based Piezoresistive Sensors for Strain Sensing Applications." *Additive Manufacturing* 20:119–125. Elsevier. https://doi.org/10.1016/j.addma.2018.01.004.

Cressie, N., and D. M. Hawkins. 1980. "Robust Estimation of the Variogram: I." *Journal of the International Association for Mathematical Geology* 12 (2): 115–125. Springer. https://doi.org/10.1007/BF01035243.

Farneti, E., N. Cavalagli, M. Costantini, F. Trillo, F. Minati, I. Venanzi, and F. Ubertini. 2023. "A Method for Structural Monitoring of Multispan Bridges Using Satellite InSAR Data with Uncertainty Quantification and Its Pre-Collapse Application to the Albiano-Magra Bridge in Italy." *Structural Health Monitoring* 22 (1). 353–371. SAGE Publications Sage UK: London, England. https://doi.org/10.1177/14759217221083609.

Hsu, R. 1999. "An Alternative Expression for the Variance Factors in Using Iterated Almost Unbiased Estimation." *Journal of Geodesy* 73 (4): 173–179. Springer. https://doi.org/10.1007/s001900050234.

Hu, C., Y. K. Deng, W. M. Tian, and J. Y. Wang. 2019. "A PS Processing Framework for Long-Term and Real-Time GB-SAR Monitoring." *International Journal of Remote Sensing* 40 (16): 6298–6314. Taylor & Francis. https://doi.org/10.1080/01431161.2019.1590876.

Huang, Q. H., Y. Wang, G. Luzi, M. Crosetto, O. Monserrat, J. F. Jiang, H. W. Zhao, and Y. L. Ding. 2020. "Ground-Based Radar Interferometry for Monitoring the Dynamic Performance of a Multitrack Steel Truss High-Speed Railway Bridge." *Remote Sensing* 12 (16): 2594. https://doi.org/10.3390/rs12162594.

Ji, P. F., X. L. Lv, Q. Chen, G. C. Sun, and J. C. Yao. 2020. "Applying InSAR and GNSS Data to Obtain 3-D Surface Deformations Based on Iterated Almost Unbiased Estimation and Laplacian Smoothness Constraint." *IEEE Journal of Selected Topics in Applied Earth Observations & Remote Sensing* 14:337–349. IEEE. https://doi.org/10.1109/JSTARS.2020.3040317.

Jiang, R. N., D. V. Jáuregui, and K. R. White. 2008. "Close-Range Photogrammetry Applications in Bridge Measurement: Literature Review." *Measurement* 41 (8): 823–834. Elsevier. https://doi.org/10.1016/j.measurement.2007.12.005.

Lebrenz, H. N., and A. Bárdossy. 2017. "Estimation of the Variogram Using Kendall's Tau for a Robust Geostatistical Interpolation." *Journal of Hydrologic Engineering* 22 (9): 04017038. American Society of Civil Engineers. https://doi.org/10.1061/(ASCE)HE.1943-5584.0001568.

Li, Q. Q., R. Chen, W. Tu, Z. P. Chen, B. C. Zhang, A. G. Yan, and P. C. Yin. 2023. "Real-Time Vision-Based Deformation Measurement of Long-Span Bridge with Inertial Sensors." *Geomatics and Information Science of Wuhan University* 48 (11): 1834–1843. https://doi.org/10.13203/j.whugis20230006.

Liu, J. H., J. Hu, Z. W. Li, J. J. Zhu, Q. Sun, and J. Gan. 2017. "A Method for Measuring 3-D Surface Deformations with InSAR Based on Strain Model and Variance Component Estimation." *IEEE Transactions on Geoscience & Remote Sensing* 56 (1): 239–250. IEEE. https://doi.org/10.1109/TGRS.2017.2745576.

Long, S. C., W. T. Liu, J. Y. Ma, A. X. Tong, W. H. Wu, and C. G. Zhu. 2022. "Health Monitoring and Safety Evaluation of Bridge Dynamic Load with a Ground-Based Real Aperture Radar." *Survey Review* 54 (383): 172–186. https://doi.org/10.1080/00396265.2021.1920792.

Lowry, B., F. Gomez, W. Zhou, M. A. Mooney, B. Held, and J. Grasmick. 2013. "High Resolution Displacement Monitoring of a Slow Velocity Landslide Using Ground Based Radar Interferometry." *Engineering Geology* 166 (November): 160–169. https://doi.org/10.1016/j.enggeo.2013.07.007.

Lu, P., Z. J. Xu, Y. R. Chen, and Y. T. Zhou. 2020. "Prediction Method of Bridge Static Load Test Results Based on Kriging Model." *Engineering Structures* 214:110641. Elsevier. https://doi.org/10.1016/j.engstruct.2020.110641.

Lucas, J. R. 1985. "A Variance Component Estimation Method for Sparse Matrix Applications." https://repository.library.noaa.gov/view/noaa/55445.

Luzi, G., M. Pieraccini, D. Mecatti, L. Noferini, G. Macaluso, A. Tamburini, and C. Atzeni. 2007. "Monitoring of an Alpine Glacier by Means of Ground-Based SAR Interferometry." *IEEE Geoscience & Remote Sensing Letters* 4 (3): 495–499. IEEE. https://doi.org/10.1109/LGRS.2007.898282.

Mardia, K. V., C. Goodall, E. J. Redfern, and F. J. Alonso. 1998. "The Kriged Kalman Filter." *Penetotester6* 7 (2): 217–282. Springer. https://doi.org/10.1007/BF02565111.

Miccinesi, L., A. Beni, and M. Pieraccini. 2021. "Multi-Monostatic Interferometric Radar for Bridge Monitoring." *Electronics* 10 (3): 247. MDPI. https://doi.org/10.3390/electronics10030247.

Miccinesi, L., and M. Pieraccini. 2020. "Bridge Monitoring by a Monostatic/Bistatic Interferometric Radar Able to Retrieve the Dynamic 3D Displacement Vector." *Institute of Electrical and Electronics Engineers Access* 8:210339–210346. IEEE. https://doi.org/10.1109/ACCESS.2020.3039381.

Michel, C., and S. Keller. 2021. "Advancing Ground-Based Radar Processing for Bridge Infrastructure Monitoring." *Sensors (Switzerland)* 21 (6): 2172. MDPI. https://doi.org/10.3390/s21062172.

Oliver, M. A., and R. Webster. 2014. "A Tutorial Guide to Geostatistics: Computing and Modelling Variograms and Kriging." *Catena* 113:56–69. Elsevier. https://doi.org/10.1016/j.catena.2013.09.006.

Pieraccini, M., M. Fratini, F. Parrini, G. Macaluso, and C. Atzeni. 2004. "High-Speed CW Step-Frequency Coherent Radar for Dynamic Monitoring of Civil Engineering Structures." *Electronics Letters* 40 (14): 907–908. The Institution of Engineering & Technology. https://doi.org/10.1049/el:20040549.

Psimoulis, P. A., and S. C. Stiros. 2013. "Measuring Deflections of a Short-Span Railway Bridge Using a Robotic Total Station." *Journal of Bridge Engineering* 18 (2): 182–185. American Society of Civil Engineers. https://doi.org/10.1061/(ASCE)BE.1943-5592.0000334.

Qiu, D. W., Y. Z. Wang, Y. L. Zhang, Y. Tong, H. R. Liang, K. L. Ding, S. S. Wan, and J. Wang. 2023. "Settlement Monitoring Data Fusion Approach for High-Speed Railways Based on GNSS and InSAR." *Journal of Applied Remote Sensing* 17 (3): 034507–034507. Society of Photo-Optical Instrumentation Engineers. https://doi.org/10.1117/1.JRS.17.034507.

Qiu, Z. W., M. L. Jiao, T. C. Jiang, and L. Zhou. 2020. "Dam Structure Deformation Monitoring by GB-InSAR Approach." *Institute of Electrical and Electronics Engineers Access* 8 (123287–123296). IEEE:. https://doi.org/10.1109/ACCESS.2020.3005343.

Rashidi, M., M. Mohammadi, S. S. Kivi, M. M. Abdolvand, L. Truong-Hong, and B. Samali. 2020. "A Decade of Modern Bridge Monitoring Using Terrestrial Laser Scanning: Review and Future Directions." *Remote Sensing* 12 (22): 3796. MDPI. https://doi.org/10.3390/rs12223796.

Sekiya, H., K. Kimura, and C. Miki. 2016. "Technique for Determining Bridge Displacement Response Using MEMS Accelerometers." *Sensors (Switzerland)* 16 (2): 257. MDP. https://doi.org/10.3390/s16020257.

Shah, A., J. I. Bangash, A. W. Khan, I. Ahmed, A. Khan, A. Khan, and A. Khan. 2022. "Comparative Analysis of Median Filter and Its Variants for Removal of Impulse Noise from Gray Scale Images." *Journal of King Saud University - Computer and Information Sciences* 34 (3): 505–519. Elsevier. https://doi.org/10.1016/j.jksuci.2020.03.007.

Talich, M., J. Havrlant, L. Soukup, T. Plachý, M. Polák, F. Antoš, P. Ryjáček, and V. Stančík. 2023. "Accuracy Analysis and Appropriate Strategy for Determining Dynamic and Quasi-Static Bridge Structural Response Using Simultaneous Measurements with Two Real Aperture Ground-Based Radars." *Remote Sensing* 15 (3): 837. MDPI. https://doi.org/10.3390/rs15030837.

Teunissen, P. J., and A. Amiri-Simkooei. 2008. "Least-Squares Variance Component Estimation." *Journal of Geodesy* 82:65–82. Springer. https://doi.org/10.1007/s00190-007-0157-x.

Vurpillot, S., G. Krueger, D. Benouaich, and D. Clément. 1998. "Vertical Deflection of a Pre-Stressed Concrete Bridge Obtained Using Deformation Sensors and Inclinometer." *Journal of ACI Structural Journal* 95:518–526. https://doi.org/10.14359/566.

Wang, C. S., L. Chang, X. S. Wang, B. C. Zhang, and A. Stein. 2024. "Interferometric Synthetic Aperture Radar Statistical Inference in Deformation Measurement and Geophysical Inversion: A Review." *IEEE Geoscience and Remote Sensing Magazine*, IEEE. https://doi.org/10.1109/MGRS.2023.3344159.

Werner, C., T. Strozzi, A. Wiesmann, and U. Wegmüller. 2008. "GAMMA's Portable Radar Interferometer." 1–10. https://www.gamma-rs.ch/uploads/media/Instruments_Info/GPRI/references/werner08.pdf.

Wu, S. B., B. C. Zhang, X. L. Ding, L. Zhang, Z. J. Zhang, and Z. Y. Zhang. 2023. "Radar Interferometry for Urban Infrastructure Stability Monitoring: From Techniques to Applications." *Sustainability* 15 (19): 14654. MDPI. https://doi.org/10.3390/su151914654.

Xia, H., and N. Zhang. 2005. "Dynamic Analysis of Railway Bridge Under High-Speed Trains." *Computers & Structures* 83 (23): 1891–1901. Elsevier. https://doi.org/10.1016/j.compstruc.2005.02.014.

Xin, J. Z., J. T. Zhou, S. X. Yang, X. Q. Li, and Y. Wang. 2018. "Bridge Structure Deformation Prediction Based on GNSS Data Using Kalman-ARIMA-GARCH Model." *Sensors (Switzerland)* 18 (1): 298. MDPI:. https://doi.org/10.3390/s18010298.

Xu, Y. L., and Y. Xia. 2011. *Structural Health Monitoring of Long-Span Suspension Bridges*. CRC Press. https://doi.org/10.1201/b13182.

Zhang, B. C., X. L. Ding, M. Jiang, B. Zhang, S. B. Wu, and H. Y. Liang. 2016. "Ground-Based Interferometric Radar for Dynamic Deformation Monitoring of the Ting Kau Bridge in Hong Kong." 6875–6878. IEEE. https://doi.org/10.1109/IGARSS.2016.7730794.

Zhang, B., X. L. Ding, C. Werner, K. Tan, B. Zhang, M. Jiang, J. W. Zhao, and Y. L. Xu. 2018. "Dynamic Displacement Monitoring of Long-Span Bridges with a Microwave Radar Interferometer." *ISPRS Journal of Photogrammetry &*

Remote Sensing 138 (April): 252–264. https://doi.org/10.1016/j.isprsjprs.2018.02.020.

Zhang, G. J., Z. Y. Wang, W. G. Sang, B. X. Zhou, Z. W. Wang, G. B. Yao, and J. X. Bi. 2023. "Research on Dynamic Deformation Laws of Super High-Rise Buildings and Visualization Based on GB-RAR and LiDAR Technology." *Remote Sensing* 15 (14): 3651. MDPI. https://doi.org/10.3390/rs15143651.

Zhao, J. W., J. C. Wu, X. L. Ding, and M. Z. Wang. 2017. "Elevation Extraction and Deformation Monitoring by Multitemporal InSAR of Lupu Bridge in Shanghai." *Remote Sensing* 9 (9): 897. MDPI. https://doi.org/10.3390/rs9090897.

Zhu, Y., B. Xu, Z. W. Li, J. X. Hou, and Q. J. Wang. 2021. "Monitoring Bridge Vibrations Based on GBSAR and Validation by High-Rate GPS Measurements." *IEEE Journal of Selected Topics in Applied Earth Observations & Remote Sensing* 14:5572–5580. https://doi.org/10.1109/JSTARS.2021.3083494.